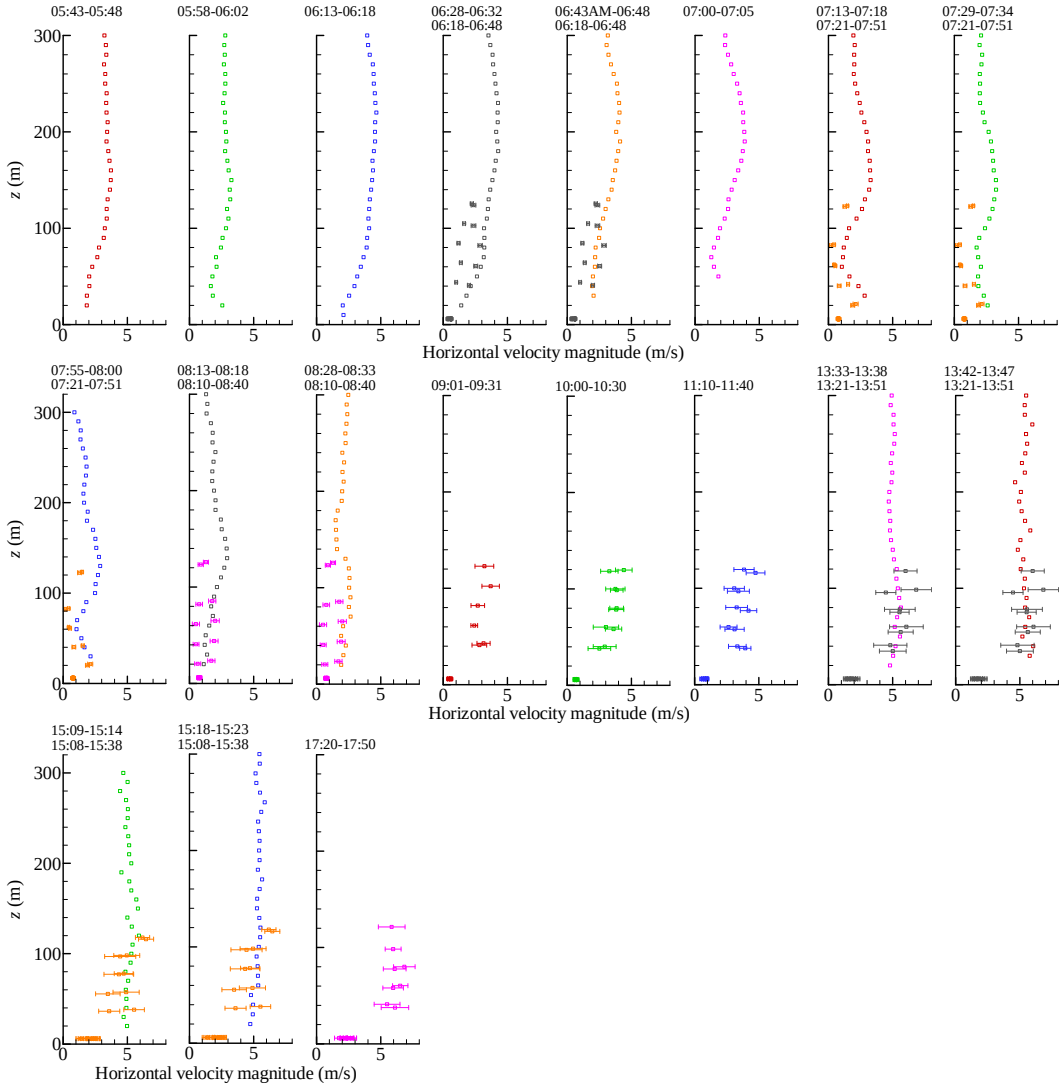

Figure 3. Profiles of horizontal velocity magnitude measured from 05:43 to 17:20. Times listed on top of each figure indicate flight time for rotorcraft, times below that indicate flight time of fixed wing aircraft.

RELATIVE STATISTICS

To obtain relative statistics, data from the straight-line flight path was used. To do this, the coordinate system was re-oriented to x_i, in which $i = 1$ was the component in the flight direction and parallel to the ground, $i = 2$ was the horizontal component perpendicular to the flight direction and $i = 3$ was in the vertical direction. Typically, twenty passes of 1200 m were flown and each straight line segment of each pass was treated as a member of an ensemble, allowing calculation of ensemble-averaged statistics. To account for the advection of the flow, Taylor's hypothesis was applied whereby for each pass the mean wind velocity U_i was calculated for each member of the ensemble and a second coordinate system was determined such that $x_i^* = x_i - U_i t$.

To calculate the auto-correlation, $R_{11}(r_1)$, the mean wind velocity was first subtracted to find u_1, then $\langle u_1(x_1)u_1(x_1 + r_1)\rangle / \langle u_1(x_1)^2\rangle$ was calculated where x_1 indicates the location along the flight path, and r_1 all possible separation distances. Here the $\langle\rangle$ brackets indicate averaging over all values of x_1 and for all members of the ensemble. A similar process was used to calculate $R_{22}(r_1)$ and $R_{33}(r_1)$ with the calculation repeated for x_i^* and r_i^*. The resulting correlations are provided in Fig. 4.

The correlations show the expected monotonic decrease with increasing r_1, although at higher values of r_1 there is increased scatter in the correlations due to decreased statistical convergence. As the boundary layer transitioned from neutrally stable towards being convective, the region of correlation increased. As a result, the longitudinal integral scales, $L_{11} = \int R_{11} dr_1$ increased from approximately 30 m to 90 m between 08:00 and 15:30. The increase in L_{11}/z from 0.6 to 1.8 reflects the increased formation of long-wavelength structures. despite the increase in convective activity and proximity to the surface. The lateral scales increased as well, with $L_{33} \approx 0.5L_{11}$ and $L_{22} \approx 0.8L_{11}$. Note that, as shown in Figure 4, there is no significant difference between the correlations calculated in the x_i and x_i^* coordinate systems, suggesting that the correction for advection had little impact on this statistic.

The longitudinal structure functions were also calculated using $S_n = \langle [u_1(x_1) - u_1(x_1 + r_1)]^n \rangle$, following the same procedure as the correlations. Although the structure functions not presented here due to space limitations, this calculation allowed the mean dissipation rate, ε to be estimated from Kolmogorov's 4/5 law by finding the average value of $\varepsilon = -1.2S_3/r_1$ over a range of 0.5 m$< r_1 <$ 15 m. In turn, the dissipation rate then allowed estimation of the Taylor microscale Reynolds number, which was found to be $Re_\lambda \approx 7 \times 10^3$, 4×10^4, 5×10^4, and 5×10^4 for each of the four flights.

Figure 4. Autocorrelations (a) R_{11}; (b) R_{22}; and (c) R_{33} calculated for each flight. Dotted lines indicate values calculated from the x_i coordinate system and solid lines indicate the values calculated from the x_i^* coordinate system.

Having an estimate of the dissipation rate also allowed calculation of the Kolmogorov scale $\eta = (\nu^3/\varepsilon)^{1/4}$, and thus allowed Kolmogorov scaling of the wavenumber spectra, which are shown in Fig. 5. To calculate these spectra, the wavenumber was estimated as $k_1 = 2\pi/r_1$. The spectra calculated from each flight leg were then ensemble-averaged to produce the resulting one-dimensional wavenumber spectra $E_{11}(k_1)$, $E_{22}(k_1)$, $E_{33}(k_1)$ for all three components of velocity. Also shown in Fig. 5 are the same spectra calculated in the x_i^* coordinate system. The results show little difference between spectra calculated with an assumed advection and without assuming advection of the flow field, but do reveal two to three decades of inertial subrange range having a $k_1^{-5/3}$ decay. Note that the decay observed in Fig. 5 at the highest wavenumbers presented does not reflect dissipation, but is instead the filtering introduced by the five-hole probe due to its limited frequency response.

The roll-off in the inertial subrange is emphasized in the compensated spectra shown in Figure 6. The expected broadening of the inertial subrange with increasing Reynolds number becomes readily apparent. Although the lower wavenumbers show evidence of incomplete statistical convergence, the higher wavenumbers are in broad agreement with Kolmogorov's constants, indicated by dashed lines. These compensated spectra suggested that at the lowest Re_λ, most of the energy containing eddy range was captured by the 1200 m flight path. However, as Re_λ increased, the low wavenumber range became increasingly less resolved.

Conclusions

The results presented here demonstrate that it is possible to obtain high-Reynolds-number turbulence data in the atmospheric boundary layer using unmanned aerial vehicles. As these vehicles are traveling at velocities an order of magnitude faster than the wind velocity, the statistics are effectively being measured in space, rather than time. This is illustrated in the reduced impact of Taylor's hypothesis on the statistics, which manifests in only minor differences at large separations. Limitations in the approach of using UAVs appears as decreased statistical convergence at longer separation distances, and through the limited frequency response of the five-hole probe. Improvements are currently being made in the measurement system to improve these qualities.

During the measurements, which were conducted during a morning transition from stable to unstable conditions, autocorrelations, structure functions, and spectra were successfully measured. These results showed that during this period, at $z = 50$ m, the Taylor microscale Reynolds number increased by an order of magnitude from $Re_\lambda \approx 7 \times 10^3$ to 5×10^4 and the longitudinal integral scales increased from 30 m to 90 m. The spectra measured over this period showed an order of magnitude increase in the wavenumber range of the inertial subrange, with the subrange constants in rough agreement with the Kolmogorov predictions.

Acknowledgments

This work was supported by the National Science Foundation through grant #CBET-1351411 and by National Science Foundation award #1539070, Collaboration Leading Operational UAS Development for Meteorology and Atmospheric Physics (CLOUDMAP). The authors would like to thank Ryan Nolin, Caleb Canter, Jonathan Hamilton, Elizabeth Pillar-Little, William Sanders, and Robert Singler who worked tirelessly to build, maintain, and fly the unmanned vehicles used in this study.

REFERENCES

del Álamo, J.C. & Jiménez, J. 2009 Estimation fo turbulent convection velocities and corrections to taylor's approximation. *J. Fluid Mech.* **640**, 5–26.

Dhanak, M.R. & Holappa, K. 1999 An autonomus ocean turbulence measurement platform. *Journal of Atmospheric and Oceanic Technology* **16**, 1506–1518.

Eberhard, W.L., Cupp, R.E. & Healey, K.R. 1989 Doppler lidar measurement of profiles of turbulence and momentum flux. *J. Atmos. Oceanic Technol.* **6**, 809–819.

Eheim, C., Dixon, C., Agrow, B.M. & Palo, S. 2002 Tornado chaser: A remotely-piloted UAV for in situ meteorological measurements. In *AIAA Paper 2002-3479, 1st AIAA Unmanned Aerospace Vehicles, Systems, Technologies, and Operations Conference and Workshop*.

Grant, H. L., Stewart, R. W. & Moilliet, A. 1962 Turbulence spectra from a tidal channel. *J. Fluid Mech.* **12**, 241–268.

Guala, M., Metzger, M. & McKeon, B. 2011 Interactions within the turbulent boundary layer at high Reynolds number. *J. Fluid Mech.* **666**, 573–604.

Higgins, C.W., Froidevaux, M., Simeonov, V., Vercauteren, N., Barry, C. & Parlange, M.B. 2012 The effect of scale on the applicability of taylors frozen turbulence hypothesis in the atmospheric boundary layer. *Boundary-Layer Meteorol.* **143**, 379–391.

van den Kroonenberg, A., Martin, T., Buschmann, M., Bange, J. & Vörsmann, P. 2008 Measuring the wind vector using the autonomous mini aerial vehicle M^2AV. *J. Atmos. Oceanic Technol.* **25**, 1969–1982.

Lenschow, D.H. & Johnson, W.B. 1968 Concurrent airplane and balloon measurments of atmospheric boundary layer structure over a forest. *J. Appl. Meteor.* **7**, 79–89.

Levine, E. R. & Lueck, R.G. 1999 Turbulence measurements from an autonomous underwater vehicle. *Journal of Atmospheric and Oceanic Technology* **16**, 1533–1544.

Matvev, V., Dayan, U., Tass, I. & Peleg, M. 2002 Atmospheric sulfur flux rates to and from israel. *The Science of the Total Environment* **291**, 143–154.

Mayer, S, Jonassen, M, Sandvik, A & Reuder, J 2012 Atmospheric profiling with the UAS SUMO: a new perspective for the evalu-

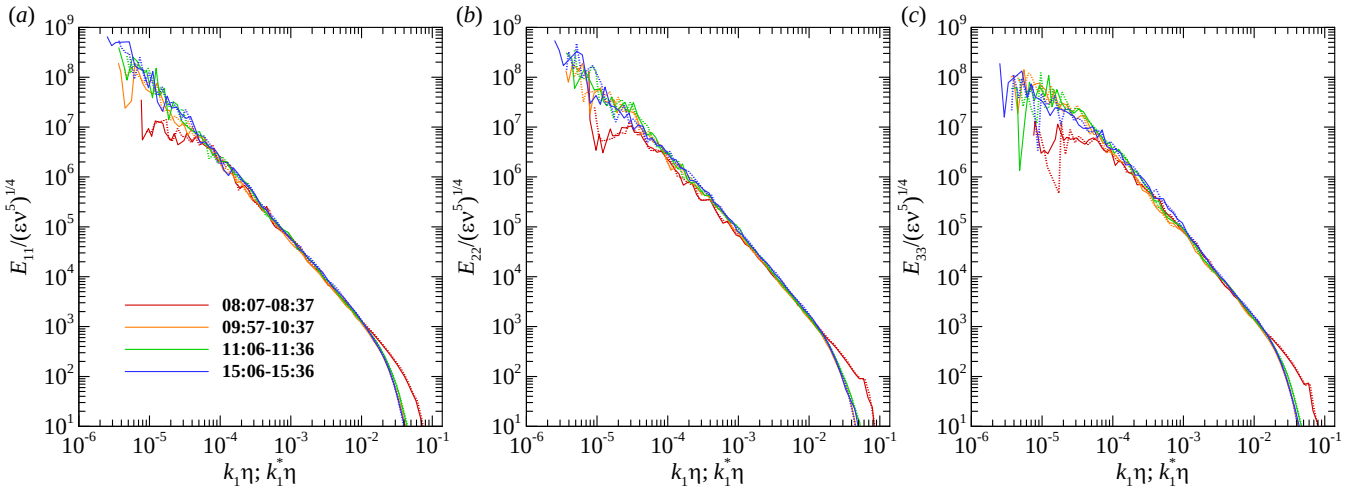

Figure 5. Scaled power spectra (a) $E_{11}(k_1)$; (b) $E_{22}(k_1)$; and (c) $E_{33}(k_1)$ calculated for each flight. Dotted lines indicate values calculated from the x_i coordinate system and solid lines indicate the values calculated from the x_i^* coordinate system.

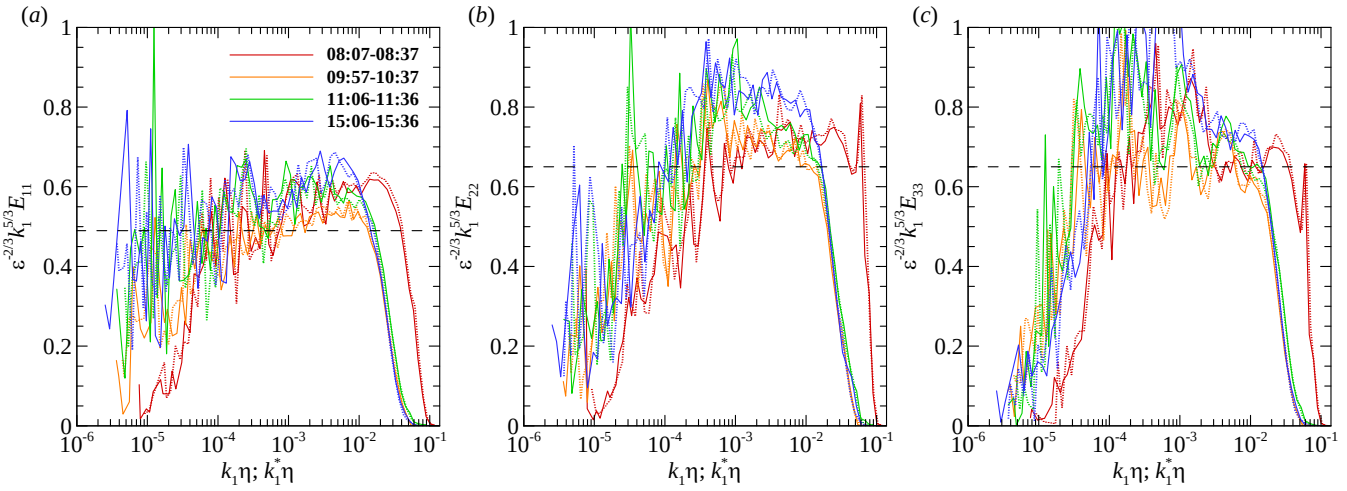

Figure 6. Compensated power spectra (a) $E_{11}(k_1)$; (b) $E_{22}(k_1)$; and (c) $E_{33}(k_1)$ calculated for each flight. Dotted lines indicate values calculated from the x_i coordinate system and solid lines indicate the values calculated from the x_i^* coordinate system.

ation of fine-scale atmospheric models. *Meteorology and Atmospheric Physics* **116** (1–2), 15–26.

Metzger, M. & Holmes, H. 2008 Time scales in the unstable atmospheric surface layer. *Boundary-Layer Meteorol.* **126**, 29–50.

Metzger, S., Junkermann, W., Butterbach-Bahl, K., Schmid, H. P. & Foken, T. 2011 Measuring the 3-d wind vector with a weight-shiftmicrolight aircraft. *Atmos. Meas. Tech.* **4**, 1421–1444.

Monty, J.P., Hutchins, N., Ng, H.C.H., Marusic, I. & Chong, M.S. 2009 A comparison of turbulent pipe, channel and boundary layer flows. *J. Fluid Mech.* **632**, 431–442.

Neumann, P. P. & Bartholmai, M. 2015 Real-time wind estimation on a micro unmanned aerial vehicle using its internal measurement unit. *Sensors and Actuators A: Physical* **235**, 300310.

Palomaki, Ross T., Rose, Nathan T., van den Bossche, Michael, Sherman, Thomas J. & Wekker, Stephan F.J. De 2017 Wind estimation in the lower atmosphere using multi-rotor aircraft. *Journal of Atmospheric and Oceanic Technology* **Early online release**.

Payne, F.R. & Lumley, J.L. 1966 One-dimensional spectra derived from an airborne hot-wire anemometer. *Quarterly Journal of the Royal Meteorological Society* **92**, 397–401.

Philbrick, C.R. 2002 Raman lidar descriptions of lower atmosphere processes. In *Proceedings of the 21st ILRC, Valcartier, Quebec Canada*, p. 535545.

Sheih, C. M., Tennekes, H. & Lumley, J.L. 1971 Airborne hot-wire measurements of the small-scale structure of atmospheric turbulence. *Phys. Fluids* **14** (2), 201–215.

Taylor, G. I. 1938 The spectrum of turbulence. *Proc. R. Soc. Lond.* **164** (919), 476–490.

Thorpe, S. A., Osborn, T. R., Jackson, J. F. E., Hall, J. & Lueck, R. G. 2003 Measurements of turbulence in the upper-ocean mixing layer using Autosub. *Journal of Physical Oceanography* **33**, 122–145.

Treviño, G. & Andreas, E.L. 2008 On reynolds averaging of turbulence time series. *Boundary-Layer Meteorol.* **128**, 303–311.

Zaman, K.B.M.Q & Hussain, A.K.M.F 1981 Taylor hypothesis and large-scale coherent structures. *J. Fluid Mech.* **112**, 379–396.